Mechanical Systems and Signal Processing 158 (2021) 107758

Contents lists available at ScienceDirect

Mechanical Systems and Signal Processing

journal homepage: www.elsevier.com/locate/ymssp

Application of fibre optic sensing systems to measure rotor blade structural dynamics

Simone Weber [a,c], Thomas Kissinger [b], Edmond Chehura [b], Stephen Staines [b], James Barrington [b], Kevin Mullaney [b], Luca Zanotti Fragonara [d], Ivan Petrunin [d], Stephen James [b], Mudassir Lone [c], Ralph Tatam [b,*]

[a] Airbus Helicopters UK Ltd., 128 Langford Ln, Kidlington OX5 1QZ, United Kingdom
[b] Cranfield University, Centre for Engineering Photonics, Cranfield MK43 0AL, United Kingdom
[c] Cranfield University, Centre for Aeronautics, Cranfield MK43 0AL, United Kingdom
[d] Cranfield University, Centre for Autonomous and Cyberphysical Systems, Cranfield MK43 0AL, United Kingdom

ARTICLE INFO

Article history:
Received 19 September 2019
Received in revised form 12 February 2021
Accepted 13 February 2021

Keywords:
Bearingless main rotor blade
Fibre Bragg gratings
Shape measurement

ABSTRACT

This paper compares two fibre optic sensing techniques for vibration characterisation: (a) optical fibre Bragg grating (FBG) strain gauges and (b) a novel direct fibre optic shape sensing (DFOSS) approach based on differential interferometric strain measurements between multiple fibres within the same fibre arrangement. Operational mode shapes and frequency measurements of an Airbus Helicopters H135 bearingless main rotor blade (5.1 m radius) were acquired during a series of ground vibration tests undertaken in a controlled laboratory environment. Data recorded by the fibre optic instrumentation systems were validated using commercially available accelerometers and compared against a baseline finite element model. Both fibre optic sensing systems proved capable of identifying the natural frequencies of the blade in the frequency range of interest (0–100 Hz). The data from the FBG sensors exhibited a dependency on their position relative to the neutral axes of the blade, which meant that full characterisation of the flapping and lagging modes required careful consideration of sensor location in the chordwise direction. The DFOSS system was able to identify all structural dynamics, despite being located on the neutral axis in the lagging direction, due to its sensitivity to angle changes, rather than strain, and its biaxial measurement capability. The DFOSS system also allowed the operational mode shapes of the blade to be determined directly, without the requirement for strain transfer from the blade to the sensor and without the requirement for a model of the underlying structure. The accuracy of obtained natural frequencies and operational mode shapes is assessed, demonstrating the potential of the use of both fibre optic sensing systems for determining blade structural dynamics.

1. Introduction

Knowledge of the structural dynamics of helicopter rotor blades is of considerable importance to the rotorcraft community from design, performance and safety perspectives. The multi-role nature of helicopter operations means that the rotor

* Corresponding author.
E-mail address: r.p.tatam@cranfield.ac.uk (R. Tatam).

https://doi.org/10.1016/j.ymssp.2021.107758
0888-3270/

blades are required to perform over a broad flight envelope and consequently today's rotor blade designs have evolved to include complex lightweight internal structures. Overall, these factors lead to a series of challenging problems for the development of model-based design methods and for the development of validation techniques. Typically, structural modal properties, such as natural frequencies, mode shapes and damping, are characterised from ground vibration tests (GVT) [1,2]. While the collected experimental data enables the validation of finite element (FE) models, it is also important in assessing the effects of modifications of the structure and in understanding the source of in-flight abnormalities. Furthermore, there is an increasing interest in operational in-flight monitoring [3–6], which offers the potential to validate fully aeroelastic models during flight and the potential for integration with current helicopter health and usage monitoring systems to enable predictive maintenance, fatigue logging and damage detection.

While accelerometers are used widely for GVT [7–9], generally providing high-fidelity data and offering simple installation, their use for in-flight measurement is impractical. This stems from the aerodynamic impact of their housing and electrical wiring, and from the superposition of the desired vibration measurements with the signals corresponding to the centrifugal acceleration of the blade and overall helicopter movement [10]. Strain gauges have been employed in-flight [11–13] to monitor structural deformation of rotor blades. Their utility is also limited by the influence of the wiring on the aerodynamics and consequently on the dynamic behaviour of the blade. Long installation times, the requirement for high fidelity strain transfer and their sensitivity to temperature and water ingress are further limitations. Due to these difficulties, measurement points are often sparse, resulting in low spatial resolution and a requirement for interpolation of the data, compromising the validation of the aerodynamic analysis [14,15]. In addition, interpretation of the data requires a detailed structural model of the object under test to relate the measured strain changes to blade deformations [16–21]. Furthermore, it has been noted that strain gauges often fail during testing and that the quality of the data can be compromised by noise on the electrical slip rings often used to transfer the data to the fixed frame [22].

The use of optical imaging methods to determine blade dynamics has a rich history, with measurement on rotor blades dating back to as early as 1940, when a rotor hub-mounted camera was used to capture low-frequency dynamics on a rotating rotor [23, p. 87]. The data showed the value of the measurement by identifying the limitations of mathematical models that did not include the Coriolis acceleration term. Since then, a variety of non-contact optical imaging metrology approaches, such as projection Moire interferometry [24], stereo pattern recognition [25,26], digital image correlation [22,27], photogrammetry [7] and the image pattern correlation technique (IPCT) [28–30], have been shown to be effective in providing clear visualisation of the structural dynamics of rotor blades in controlled environments such as wind tunnels (with the camera generally in the stationary frame observing the passing blade). More recently, IPCT systems mounted in the rotating frame have been used successfully to measure deformations of propeller blades on a fixed wing aircraft [31] and of rotor blades during a whirl rig test [32]. While providing useful test data, such approaches present challenges for routine use resulting from the fouling of surfaces, from variations in ambient lighting and practical compromises resulting from the requirement for measurement geometries with a large observation angle and depth of field.

The potential for the use of optical fibres for monitoring aircraft structures has been well-documented [33]. They offer several key benefits, including their flexibility, low weight, electromagnetic immunity, small dimensions (diameter: $\sim$0.2 mm) and no requirement for electrical connection to the sensing elements. In addition, optical fibres can be embedded within fibre reinforced composites during fabrication [34–36], or, alternatively, can be surface-mounted to facilitate retrofitting [37–39]. Most fibre optic strain sensing techniques use fibre Bragg gratings (FBGs), which are in-fibre strain sensors of typically 0.5–5 mm gauge length [40]. FBGs represent a mature technology that is commercially available, where tens of sensors per fibre can typically be multiplexed in a single optical fibre at data rates on the order of 1 kHz and with strain resolutions of 1 $\mu m/m$. The in-flight use of FBG sensors on fixed-wing aircraft has been investigated previously [41,19,37]. More recently, their use on rotorcraft has been explored [42], with FBG strain sensors deployed on a scaled helicopter rotor operated in a wind tunnel to estimate its tip displacement by using a shape reconstruction algorithm. They have also been integrated into the root of a bearingless main rotor (BMR) blade [43], where the measured strain was used in the calculation of the useful remaining life of the blade. Recently, FBG strain sensors were used for in-flight measurements on a T-22 helicopter [44]. Here, six FBG sensors were multiplexed in a single length of optical fibre and were connected to a battery-powered interrogator located at the top of the rotor mast. The data allowed the identification of the rotor blades' dynamic characteristics in the flap (out-of-plane), lead-lag (in-plane) and torsional directions. This represented a step towards the routine use of structural health monitoring capabilities by demonstrating their potential for in-flight measurements.

A number of fibre optic-based shape sensing approaches have been reported [18–20]. The shape of a structure is the most fundamental characteristic that can be analysed and deviations from the expected shape can be easily visualised and interpreted. The majority of fibre optic shape sensing techniques rely on the measurement of the differential strain experienced by several laterally offset optical fibres mounted on opposing surfaces of the structure under test to determine local curvature, from which the shape of the structure can be determined. Such indirect FBG-based shape measurements require a detailed model of the structure, and the determination of shape could fail through inappropriate strain transfer, inaccurate positioning of sensors, the presence of thermal gradients [45], or inaccuracies of the structural model, which would be exacerbated where the structure suffers damage [46]. In recent years there has been interest in the development of the ability to measure the path followed by an optical fibre itself in three dimensions, so-called direct fibre optic shape sensing (DFOSS) [47]. DFOSS allows changes in the optical fibre's path, and thus changes in the shape of the structure to which the fibre is attached, to be measured in three dimensions. A key advantage of DFOSS is that the shape is determined directly within the sensing cable arrangement, removing the dependency on efficient strain transfer from the structure to the sensor. Simple

surface mounting, for example using adhesive tape, is sufficient for it to follow the shape of the structure. In DFOSS, there is no requirement for a detailed model of the structure and the differential nature of the DFOSS measurements makes these automatically compensated for temperature as long as there are no significant temperature gradients across the sensor diameter. If deployed within a rotating reference frame, the differential nature of the measurement underlying the shape determination will also render the DFOSS approach immune to the centrifugal forces, which would impart a longitudinal strain dependent on the rotational frequency to strain sensors such as FBGs, and would superimpose a cyclically varying signal on accelerometers. It should be noted that the response of intrinsic optical fibre sensors, including optical fibre gratings and the interferometric sensors that are the basis of the DFOSS system used here, is based on well-known optical properties of glass and has been shown to be highly linear over large strain excursions [48]. Thus the baseline loading caused by centrifugal loading is not expected to influence the measurement fidelity. Ultimately, DFOSS systems have the potential to be implemented completely within a single multi-core optical fibre (diameter: ~0.2 mm) that can be embedded into composite structures. Changes in the orientation of the cores caused by twisting during installation, which warps the measurement coordinate system, can be compensated by use of a calibration procedure [49], or by the use of multicore optical fibre with a D-shaped cross section that facilitates deployment with a known orientation [50].

This paper presents work carried out within the BladeSense project [51] and aims to investigate the feasibility of the use of FBG and DFOSS instrumentation [47] on an Airbus Helicopters H135 BMR blade to collect structural vibration data during GVT, with an ultimate view towards exploring future utility of the measurement techniques for routine in-flight blade monitoring. The determined resonant frequencies and vibration mode shapes are validated using commercially available accelerometers. Additionally, a baseline FE model was developed to allow the determination of the displacement mode shapes and surface strain mode shapes and their comparison with the operational mode shapes obtained from the optical and accelerometer measurements.

2. Methodology

2.1. Baseline model

An FE model of the BMR blade (5.1 m radius) of an H135 helicopter was developed to assist the design of the experiment in terms of sensor locations and to guide the interpretation of the data, in particular the strain data from the FBGs. The BMR blade incorporates the conventional mechanical flapping, lagging and torsional hinges into a single flexible structure. This is achieved by using a complex composite layout with varying geometrical cross-sections and material properties. As shown in Fig. 1, the blade consists of the pitch control cuff with an elastomeric lead-lag damper, an aerofoil section and a flexbeam. Detailed information about the H135 BMR blade can be found in Refs. [23,52–54].

The blade was modelled with one-dimensional beam elements and was coupled with geometric surface points to allow comparison with surface mounted sensors. Standard FE modelling techniques were adopted employing the Nastran software package [55], using a primary one-dimensional stick for the flexbeam and the blade aerofoil section, and a secondary stick parallel to the flexbeam representing the pitch control cuff. Scalar spring elements are incorporated to ensure correct coupling between the flexbeam and the pitch control cuff, and to take into account the stiffness of the rotational movement induced by the pitch control cuff. A schematic of the modelling principle is shown in Fig. 2.

The geometric surface is represented by coupling surface points with the structural dynamics model. It is assumed that the shape of the cross-section remains unaltered during deformation, regardless of the loading conditions. Warping and shear deformations of the blade profile are neglected. The non-rotating natural frequencies and mode shapes were produced using the Nastran modal analysis solver. Fig. 3 shows the first eight structural mode shapes of the rotor blade. Each plot is labelled such that 1F stands for the first flapping mode, 1L is the first lagging mode and 1T is the first torsional mode, etc. The flapping modes exhibit motion predominantly in the vertical plane, i.e. along the z-direction, and the lagging motion occurs predominantly in the horizontal plane, i.e. along the x-direction. While the first four mode shapes have a dominant flapping or lagging component, Mode 2L exhibits a coupled flapping/lagging component, Mode 1T has a coupled torsion/flapping

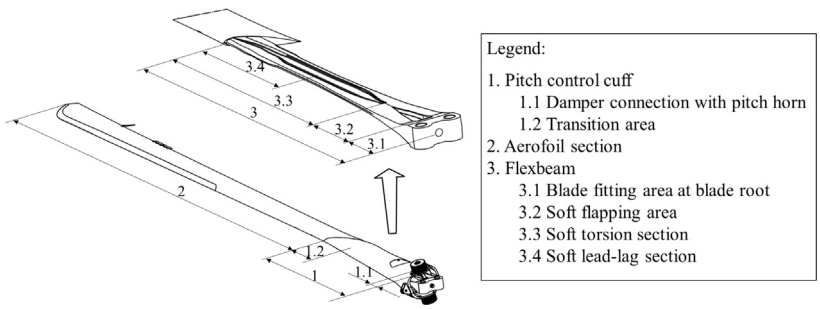

Fig. 1. BMR blade of the H135 helicopter (adapted from Bansemir et al. [53]).

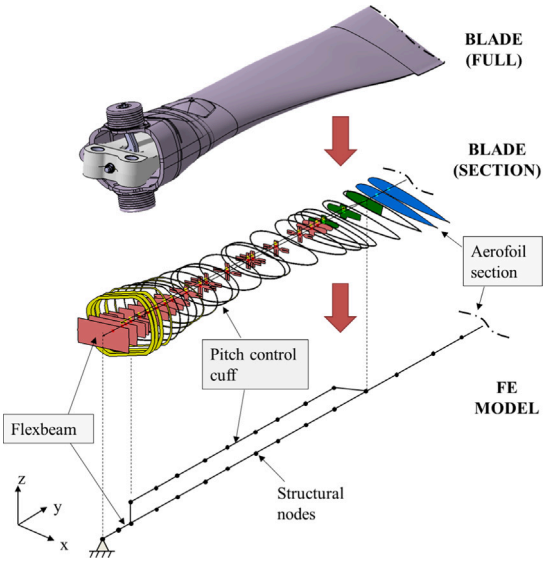

Fig. 2. Schematic of the FE modelling principle.

component, and Mode 4F has a coupled lagging/flapping component. This coupling occurs mainly due to the chord-wise locations of the centre of gravity and the shear centre [56].

Since, in this work, the FBG sensors are orientated along the blade to measure surface strain along its longitudinal axis, i.e. the y-direction in Fig. 2, a mathematical expression is formulated that calculates the axial surface strain ϵ_T in the y-direction as a function of combined flapping and lagging displacement. Shear strain is neglected and, hence, the total surface strain ϵ_T is expressed through a linear superposition of the strains due to flapping and lagging movement:

$$\epsilon_T(x,y,z,t) = -c_z(x,y,z)\frac{\partial^2 w(t)}{\partial y^2} + c_x(x,y,z)\frac{\partial^2 u(t)}{\partial y^2} \tag{1}$$

where c_z and c_x represent the distance between the location of the measurement and of the neutral axis in the z and x directions, respectively, as shown in Fig. 4. The neutral axis is defined as the axis in a cross-section of a profile where there are no longitudinal stresses or strains. Throughout this paper, the neutral axis is defined as the intersection between the neutral plane and the spanwise cross-section. The vertical neutral axis position varies along the length of the rotor blade, but it is assumed to be close to the quarter chord line (see Fig. 4), while the horizontal neutral axis is centred approximately between the upper and lower surfaces. The lack of knowledge of the exact position of the neutral axis leads to assumptions being made for the strain calculation and consequently leads to fundamental uncertainties in the mathematical model description.

The *jth* axial surface strain mode shape is obtained by replacing the curvature terms in Eq. 1 with $\frac{\partial^2 \phi_j}{\partial y^2}$:

$$\psi_{T_j}(x,y,z) = -c_z(x,y,z)\frac{\partial^2 \phi_{z_j}}{\partial y^2} + c_x(x,y,z)\frac{\partial^2 \phi_{x_j}}{\partial y^2} \tag{2}$$

where ϕ_{z_j} and ϕ_{x_j} are the *jth* mode shapes in z- and x-direction, respectively. Fig. 5 shows the top surface plot for the first 8 normalised surface strain mode shapes for strain in the y-direction. Modes 1L and 2L each have a predominant lagging component, which is evident due to the high strain values at the trailing edge resulting from the separation between surface point and the neutral axis. The sudden strain changes at 20% rotor radius, caused by the junction of the cuff with the blade, are clearly observable in Fig. 5. Furthermore, Mode 1T shows a dominant flapping component because surface strain is assumed to be a linear superposition of the flapping and lagging movements. In order to facilitate comparison with experimental test data, the numerical values are interpolated at the measurement positions.

2.2. Experimental setup

Operational modal analysis was carried out on the H135 BMR blade through a series of GVTs. For each test, the blade was excited either for 60 s using a Random-on-Random (RoR) excitation waveform over a frequency range of 0–100 Hz or at a single frequency (dwell test). The experimental setup consisted of a test bench designed to rigidly mount the rotor shaft and rotor blade, as shown in Fig. 6(a). The excitation was introduced to the blade by a shaker[1] via a stinger that was adhered to the

[1] Modal exciter type 4825 (Brüel & kJær).

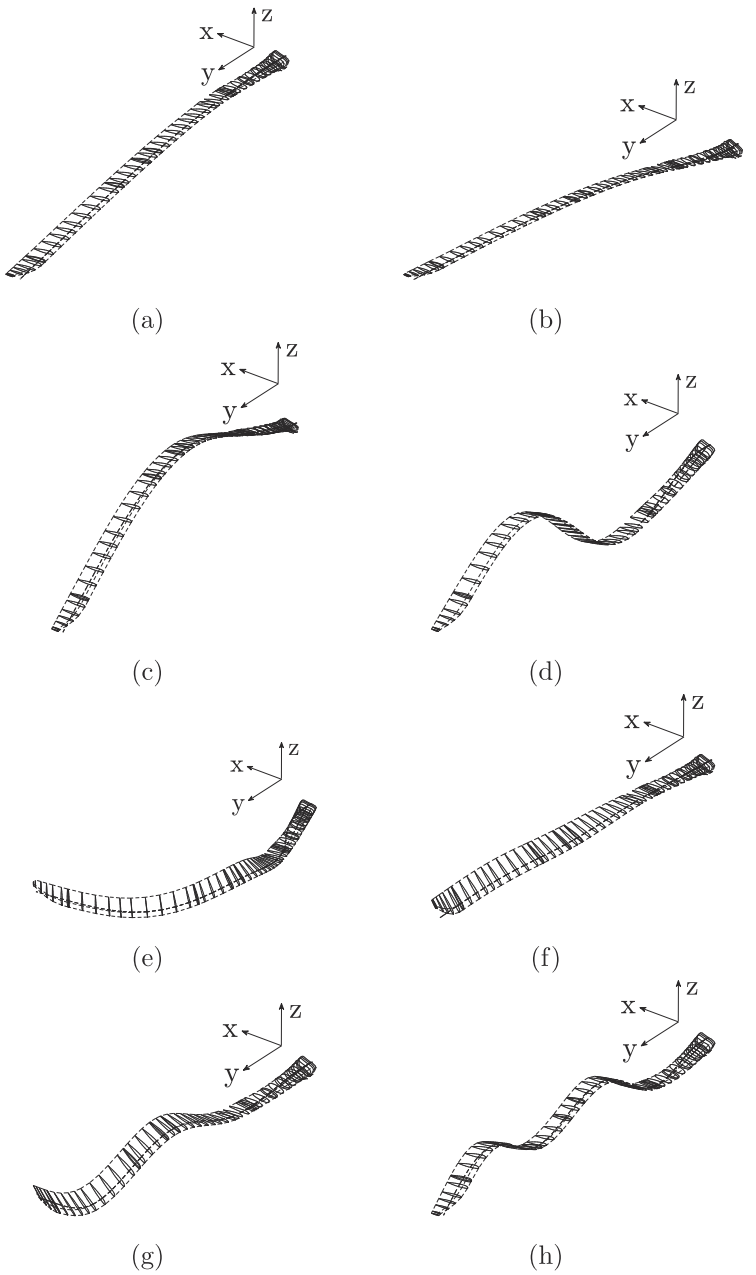

Fig. 3. The first eight displacement mode shapes ϕ: (a) 1st flapping mode (1F), (b) 1st lagging mode (1L), (c) 2nd flapping mode (2F), (d) 3rd flapping mode (3F), (e) 2nd lagging mode (2L), (f) 1st torsion mode (1T), (g) 4th flapping mode (4F), (h) 5th flapping mode (5F).

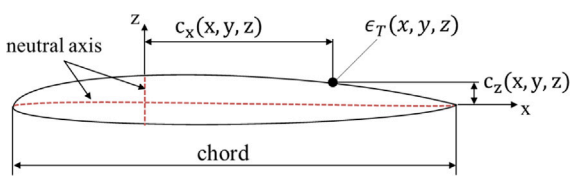

Fig. 4. Approximate locations of the neutral axes across the blade cross section.

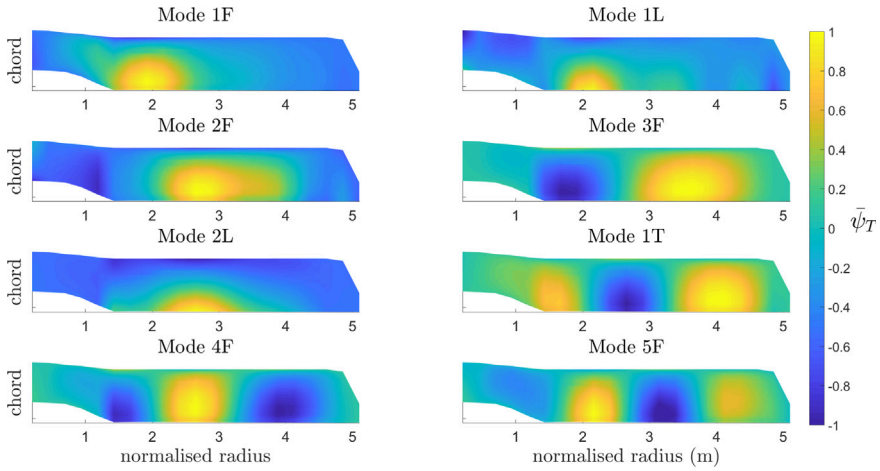

Fig. 5. Normalised surface strain mode shapes for the first eight modes for strains in the y-direction.

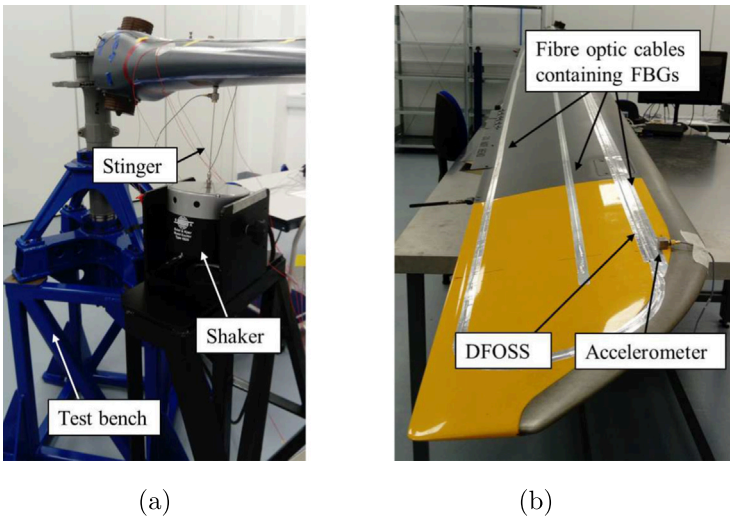

Fig. 6. The experimental setup is shown in (a). (b) depicts the mounting of the sensing elements on the blade.

pitch control cuff. Fig. 6(b) shows the sensing elements, comprising accelerometers, FBG sensor arrays and the DFOSS sensing cable, mounted on the blade.

Five uni-axial accelerometers (ACC), as shown in Fig. 7(a), each with its measurement axis oriented normal to the top surface of the blade, were located along the aerofoil quarter chord line, as was the DFOSS system. For strain measurement, a total of six optical fibres were used, three mounted on the top surface of the blade and three on the bottom surface, where corresponding fibres on the top and bottom surfaces were located at the same chordwise positions. Each optical fibre contained an array of nine wavelength-division multiplexed FBGs (see Fig. 7(b)). The chordwise locations of the optical fibres were close to the leading edge at the quarter chord line, at the half chord position, and close to the trailing edge. The FBG strain sensors were interrogated using a Smart Fibres SmartScan interrogator, which is capable of interrogating four FBG arrays, each containing up to 16 FBGs, at a data rate of 2.5 kHz, allowing 4 of the sensor arrays mounted on the blade to be monitored simultaneously. The FBGs, with centre wavelengths distributed in the 1528–1568 nm wavelength band, were fabricated in-house in hydrogen loaded SMF-28 optical fibre. The gratings were ∼5 mm in length with typical bandwidths of 0.5 nm and reflectivities of 50%. Correct bonding is important for the FBG sensors to ensure appropriate strain transfer from the structure to the sensor. The sections of fibre containing the FBG sensors were attached to the blade using a cyanoacrylate adhesive and, in order to protect the optical fibres, strips of aluminium speed tape were used to cover the length of each FBG array. Fig. 7(d) shows a cross-section of the installation of the optical fibres on the blade.

The DFOSS system, based on the fibre segment interferometry (FSI) approach [57], was described in detail by Kissinger et al. in Ref. [47]. In FSI, a pair of in-fibre partial reflectors spans a fibre segment, which each fibre segment acting as an interferometrically interrogated long gauge-length strain sensor. Typically, in FSI, multiple fibre segments are arranged back-to-

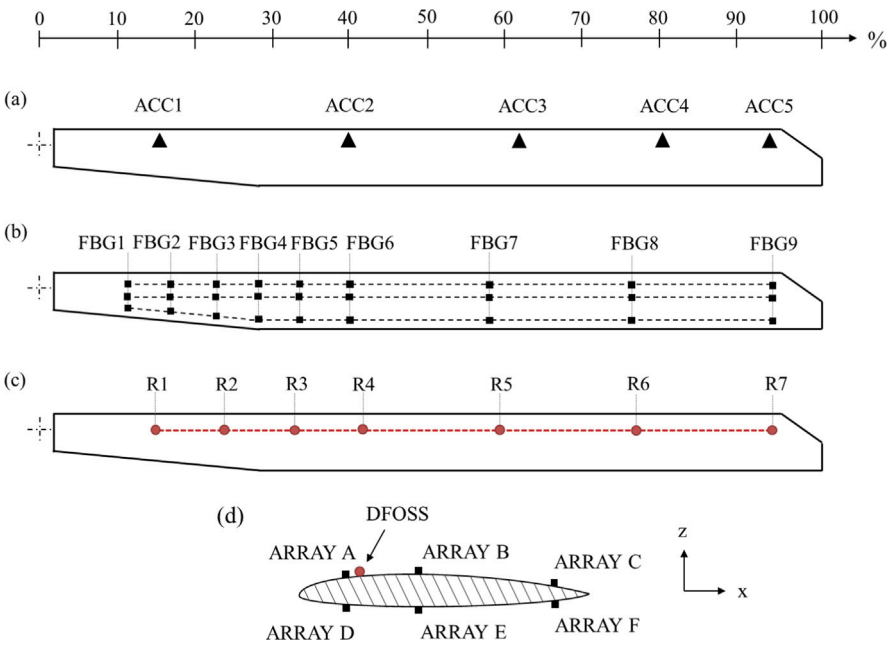

Fig. 7. The positions of the five uni-axial accelerometers (ACC) are shown in (a). The locations of the FBG arrays, with nine FBGs in each array, on the top blade surface are shown in (b). Identical chordwise locations were used for the FBG arrays on the bottom surface of the blade. The DFOSS cable with the positions of the reflectors defining the measurement sample points is shown in (c). Finally, (d) shows the cross-section of the blade, highlighting the different fibre optic cable positions along with a coordinate system defining the horizontal (x) and vertical (z) axes.

back, forming a continuous sensing chain. In contrast to regular electrical strain gauges and FBGs, the strain measurement in FSI is not localised, but is rather an integrated strain measurement over the length of each segment. There are various technologies that could be used to produce the necessary in-fibre partial reflectors, with weak, broadband FBG-based reflectors found to be a convenient choice due to the ease of inscription. It is important to note, however, that in FSI, the spectral information of the FBG-based reflectors is not analysed. Thus, the reflectors merely serve as a means to define the fibre segments, and need to be sufficiently broadband to return the light from the interrogation laser under all possible strain and temperature conditions that can occur during deployment. In this work, within each of the three optical fibres that comprise the DFOSS system, seven ultra-short ($\sim$250 μm) FBGs, of bandwidth $\sim$5 nm and reflectivity 0.01%, act as in-fibre reflectors R1 to R7 that define the boundaries of six fibre segments that form long gauge-length interferometric strain sensors. The three fibres were mounted in a 3D printed support structure designed to hold the fibres in the triangular arrangement depicted in Fig. 8(a) and (b). Care was taken to ensure that the corresponding reflectors R1 to R7 in all three fibres were co-located along the length of the support structure. Appropriate processing of the differential strains experienced by the corresponding fibre segments in the three fibres allows the direct independent measurement of the slope angle in the flapping and lagging directions [47], which is sampled at reflector locations R2 to R7 in Fig. 7(c). The slope angles are determined relative to the angle of the measurement origin of the system, which is located at reflector R1 [47]. The only assumption required to obtain the desired shape deformation data from the measured slope angle data is the use of an interpolation (using a cubic spline) between the sample points to permit spatial integration of the slope angle. Note that this interpolation method does not require knowledge of the underlying structure. For continuously bending structures like a rotor blade, the only consideration involved in defining the numbers of reflectors required is analogous to the Nyquist sampling theorem in electrical engineering, requiring that the spatial density of sample locations is sufficient to follow the expected structural bending curves.

The strains experienced by the fibre segments are interrogated using the range resolved interferometry (RRI) concept detailed in [58]. As a pseudo-heterodyne interferometric signal processing technique, RRI allows the separation of signals from multiple interferometers based on their optical path difference, i.e. their range. In RRI, the use of sinusoidal laser wavelength modulation results in range-dependent signals that can be demodulated using a unique carrier waveform for each range. After performing range-based signal separation, RRI then permits the individual demodulation of the interferometric phases of each constituent fibre segment interferometer, with the phase difference being directly proportional to the strain experienced by that fibre segment. The interrogation hardware used in RRI is very simple, typically comprising of a diode laser and a photo detector as the only active components. In the present RRI implementation, a telecommunications distributed feedback semiconductor laser diode with a centre wavelength of 1550 nm is subject to a sinusoidal injection current modulation, resulting in a concomitant sinusoidal modulation in the laser emission wavelength. Following the scheme outlined in [47], the output of the laser is split up and guided to the three sensing fibres, reflected by the array of FBG-based reflectors and guided back to a photo detector. Demodulation of the photo detector signal, undertaken in real time using

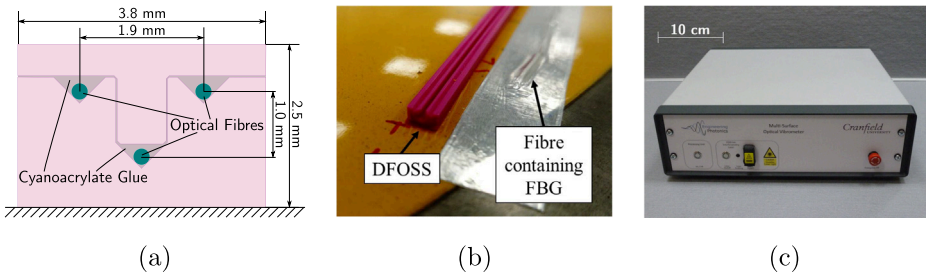

Fig. 8. DFOSS System: (a) The cross section of the sensor cable. The image in (b) was taken during the installation of the DFOSS sensor, adjacent to an FBG sensor array, (c) depicts the fully-enclosed, in-house developed interrogation unit.

a Field Programmable Gate Array (FPGA), then allows the determination of the strain experienced by each fibre segment interferometer, with very high sensitivities below nanostrain·$Hz^{-0.5}$. In line with most interferometric techniques, fibre segment interferometry can only make measurements relative to the strain experienced by the fibre when the measurement started. As a result, the current technique is more useful for dynamic measurements, where static measurements would require referencing to a known blade shape. However, for the mode shape analysis conducted in this paper only dynamic measurements are required. The fully-enclosed interrogation unit, capable of acquiring data at rates up to 49 kHz, is depicted in Fig. 8(c).

In each of the three fibres forming the cable, Fig. 8(a), the seven low reflectivity broadband FBGs in each fibre were arranged, as shown in Fig. 7(c), such that the first three segments were each of length 0.46 m and the remaining three segments were of length 0.92 m. A smaller spacing towards the root of the blade, where the flexbeam was connected to the main blade, was chosen because higher slope angle changes were expected in this region. The fibre support structure was secured to the upper surface of the blade using aluminium speed tape. Given the geometry of the fibres in the support structures and the strain resolution of the system, the angular measurement resolution is $\approx 0.2 \times 10^{-6\circ}\, Hz^{-0.5}$, approximately constant across all reflector locations R2 to R7.

3. Results & discussion

3.1. Modal properties comparison

Initially, the performances of the DFOSS, the FBG strain sensors and the uni-axial accelerometers were compared during a GVT. Each acquisition system recorded the structural response as a time series, where the sampling frequencies were 0.25 kHz for the accelerometers, 2.5 kHz for the FBGs and 1.5 kHz for the DFOSS system. Each sensor outputs data in a different physical unit: the accelerometers in m/s^2, the FBG data comprises the wavelength shift experienced by the grating, which is converted into strain using the conversion factor of 1.2 $\mu\epsilon$ pm^{-1} [59], while DFOSS provides slope angle measurements that are converted to local displacement in m using spatial integration of the interpolated slope angle curve.

The power content of the frequency spectra of the data from each technology was estimated using Welch's power spectral density (PSD) [60]. To investigate the sensitivity of each system, in all cases an RoR shaker drive force density of 0.1 N^2/Hz was chosen with a flat distribution across the chosen frequency bandwidth of 100 Hz, equating to a drive force of approximately 3 N root-mean-square. As the blade was very flexible due to the absence of centrifugal loading, this drive force was sufficient to obtain adequate data quality from the measurements. Fig. 9 compares the PSDs obtained from sensors located on the top surface at the quarter chord line at approximately 40% and 60% of the rotor radius. While sensors ACC2 and FBG6 were used for the 40% rotor radius comparison, ACC3 and FBG7 provided measurements at approximately 60% rotor radius, see Fig. 7 for exact locations. Note that the deformation curve for the DFOSS results can be obtained at arbitrary spatial resolution as a result of the continuous slope angle interpolation. Therefore, the evaluation locations of 40% and 60% rotor radius could be directly selected.

The DFOSS data was separated into vertical and horizontal components, measuring flapping and lagging movements respectively. A total of nine resonance frequencies can be observed, exhibiting agreement of the resonance frequencies determined from each sensing system. At approximately 60% rotor radius, the peaks of the ACC3 and the DFOSS system are more pronounced, while FBG6 is better able to capture structural modes at approximately 40% rotor radius. Only flapping components could be detected by the uni-axial accelerometers ACC1, ACC3, ACC4 and ACC5, while ACC2 also detected the torsion mode 1T.

The FBG sensor array located on the quarter chord line was able to measure only flapping modes, because the horizontal distance between the neutral axis and the surface was close to zero. The DFOSS system, on the other hand, was able to detect all nine resonance peaks due to its sensitivity to angular shapes (rather than surface strain), exhibiting its ability to measure biaxial components. Although exhibiting a small power content for Mode 1T, the DFOSS system was still able to detect the frequency of this mode at both radial locations. Comparing the vertical and horizontal components of the DFOSS system, a coupling between the structural modes is evident. Furthermore, a significant flapping/lagging coupling of Mode 1F was

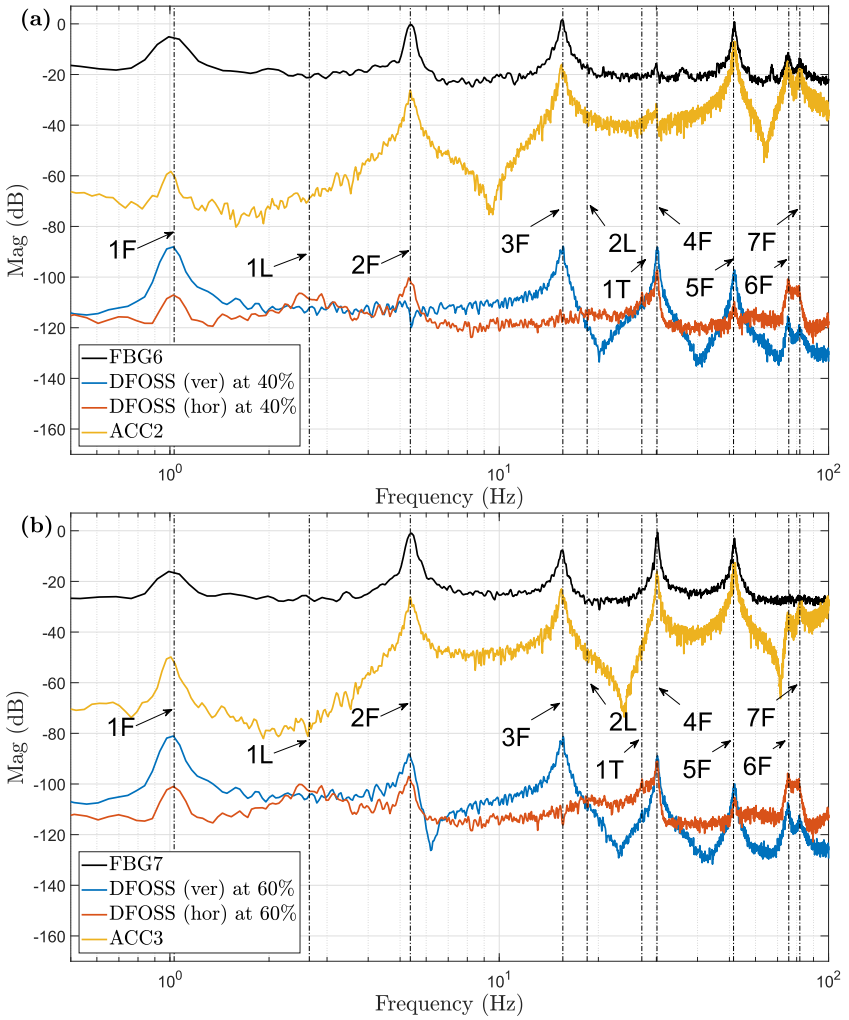

Fig. 9. Comparison of PSD measured on the top surface at quarter chord line (see also Fig. 7) at approximately 40% rotor radius shown in (a), and at approximately 60% rotor radius shown in (b), where the FBG (Array A), ACC and DFOSS spectra are mutually offset to allow easier comparison.

measured, which could have been induced by a horizontal component of the movement of the stinger. Although the lagging and torsional modes could not be detected by the FBGs located at the quarter chord line in Fig. 9, improved results were obtained from the FBGs mounted at the half chord or close to the trailing edge, Fig. 10. Measurements at the trailing edge, Arrays C and F, show that both lagging and torsional modes can be captured. On the other hand, at the half chord position, Arrays B and E, Modes 1L and 1T are barely observable. This is expected from Eq. (1), which shows that the measured strain is a function of the distance from the sensor to the neutral axis. This result also verifies the assumption that the neutral axis position for horizontal movement is approximately at the quarter chord line.

The results indicate the potential of the use of the DFOSS sensing system for capturing the resonance frequencies of all modes within the relevant frequency range by collecting data at one span-wise location. It also shows the importance of distributing the FBG arrays in an optimal manner over the surface.

Accelerometers are known to have increased sensitivity for higher frequencies, while the DFOSS system and the FBGs exhibit a flat frequency characteristic. Therefore, it can be observed that at low frequencies the DFOSS system had the highest signal-to-noise ratio, while the accelerometers offered improved performance at high frequencies.

3.2. Signal-to-noise ratio analysis

A dwell shaker test, in which the blade was excited with a constant input of 3 N at the 3rd flapping frequency of 15.72 Hz, was performed to compare the signal-to-noise ratios. The sampling frequencies during this test were 20 kHz for the accelerometers, 2.5 kHz for the FBGs and 1.5 kHz for the DFOSS system. The data obtained using the three technologies on the quarter cord line at 60% rotor radius on the top surface are shown in Figs. 11 and 12. Typical time series

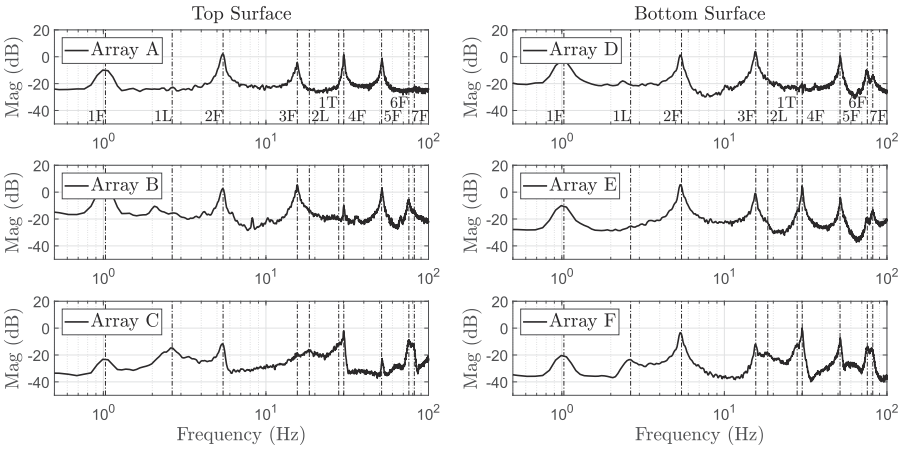

Fig. 10. PSD of three FBGs (FBG7) on both the top and bottom surfaces in chordwise direction at approximately 60% rotor radius.

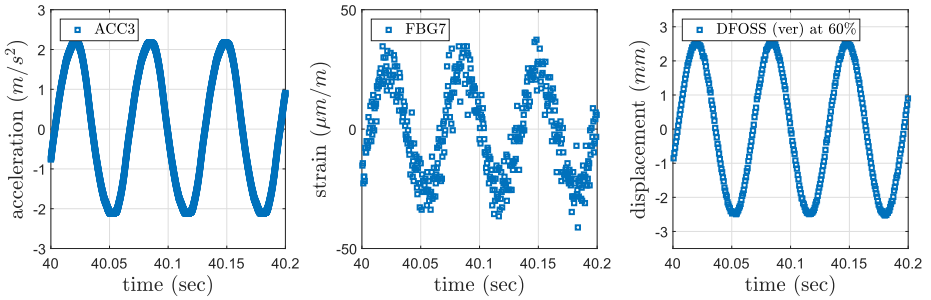

Fig. 11. Time series of raw data for 3F frequency input, collected at approximately 60% rotor radius.

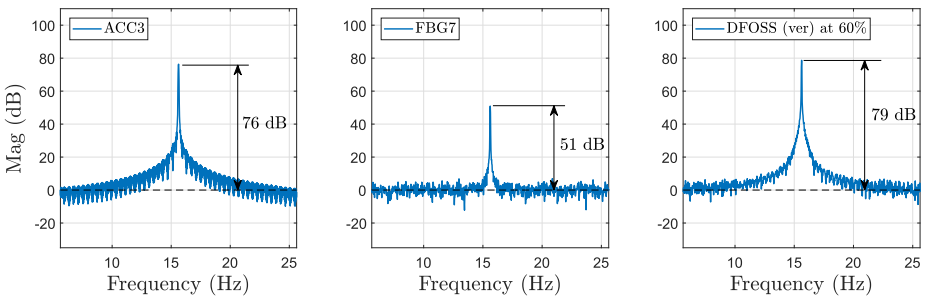

Fig. 12. Comparison of PSD for the 3F mode measured at approximately 60% rotor radius.

measurements over 0.2 s are presented in Fig. 11, while Fig. 12 shows a comparison of the PSDs calculated for this case. At this frequency, the signal-to-noise ratios of both the ACC, at 76 dB, and the DFOSS (vertical), at 79 dB, are comparable, while the signal-to-noise ratio of the FBG, at 51 dB, is considerably lower, as is also evident from Fig. 11.

3.3. Operational modal analysis comparison

From the RoR dataset that was also used in Fig. 9, the first eight natural frequencies and the corresponding damping ratios have been determined experimentally and are given in Table 1, jointly with the FE model frequencies as a reference. It was decided to run a series of tests with environmental noise as the source of the excitation, the so-called ambient vibration testing. The tests were carried out with the setup shown in Figs. 6 and 7, and a qualitative test of the whiteness and Gaussianity of the input noise was carried out, analysing the PSD response of the ACC output channel closer to the root. The operational modal analysis was carried out in the time-domain, with Stochastic Subspace Identification, using the Canonical Variate Analysis algorithm [61]. As good practice, the authors used a stabilisation diagram to determine stable poles and neglect

Table 1
Comparison of natural frequencies and damping ratios, along with standard deviations over 5 repeat measurements over a frequency range of 0–100 Hz.

Mode number	Mode type	Modal Properties						
		FE	ACC		FBG		DFOSS	
			f_n (Hz)	$\zeta(\%)$	f_n (Hz)	$\zeta(\%)$	f_n (Hz)	$\zeta(\%)$
1	1st flapping	0.90	1.02 ± 0.01	1.50 ± 0.68	1.02 ± 0.01	1.05 ± 0.16	1.03 ± 0.02	1.27± 0.92
2	1st lagging	3.41	–	–	2.60 ± 0.05	5.50± 0.02	2.64 ± 0.02	3.82± 1.46
3	2nd flapping	4.98	5.38 ± 0.03	1.44 ± 0.24	5.39 ± 0.01	1.13 ± 0.14	5.46 ± 0.02	0.85± 0.18
4	3rd flapping	15.28	15.52 ± 0.01	1.43 ± 0.22	15.44 ± 0.12	0.97 ± 0.39	15.65 ± 0.08	0.81± 0.47
5	2nd lagging	22.72	–	–	18.68 ± 0.38	–	18.51 ± 0.04	2.00± 0.24
6	1st torsion	28.59	28.37 ± 0.19	4.18 ± 3.09	27.39 ± 0.14	3.22 ± 0.48	28.08 ± 0.04	1.07 ± 0.09
7	4th flapping	29.98	30.04 ± 0.06	0.63 ± 0.14	30.17 ± 0.04	0.61 ± 0.15	30.19 ± 0.04	0.59 ± 0.11
8	5th flapping	52.17	51.84 ± 0.12	0.84 ± 0.09	51.71 ± 0.14	0.85 ± 0.29	51.70 ± 0.14	0.53 ± 0.19
9	6th flapping	75.12	75.20 ± 0.21	1.22 ± 0.46	75.68 ± 0.00	0.94 ± 0.47	75.78 ± 0.05	1.07 ± 0.12
10	7th flapping	81.80	81.58 ± 0.43	1.22 ± 0.73	81.63 ± 0.34	1.50 ± 0.21	81.84 ± 0.23	2.29 ± 0.00

mathematical or spurious modes. The "hard" stabilisation criteria were set as 0.5% for frequencies, 5% for damping, and 0.95 for the Modal Assurance Criterion (MAC) [1]. It was also ensured that only poles having damping values lying between 0 and 5% could be considered as stable, hence introducing an engineering exclusion criteria neglecting negative damping ratios or unrealistically high damping values for the blade. The stabilisation diagrams have been evaluated for a system order ranging from 50 to 100. Representative examples of stabilisation diagrams are shown in Fig. 13. Finally, results were picked by an expert operator selecting the order showing a good compromise between complexity and residual value. An automated clustering procedure was also used as a benchmark and led to similar results, as defined in [62]. In order to quantify the uncertainty of the estimations, each measurement was repeated five times, from which a mean value was formulated and error bounds calculated. It is worth highlighting that the procedure has been repeated identically for ACC, FBG and DFOSS measurements. The only difference concerned the pre-processing operations, where the FBG and DFOSS signals were subsampled to match the sampling frequency of the ACC signals.

For the frequency estimation, the standard deviation is below ±0.23 Hz for most cases, although there are a few exceptions visible, especially for weakly-excited modes. Nevertheless, this outcome contributes to the confidence in both the FBG and DFOSS measurements. The damping values, which are notoriously more affected by variance problems, show also a degree of consistency for the various sensors. In some cases, such as the torsional mode, the ACC measurement provided an unreliable estimate of the damping. This is probably due to the nature of the measurement: torsion is easier to observe using a strain gauge than by observing accelerations directly if the sensor placement is not carried out specifically to detect section rotations. Furthermore, from Table 1 it is evident that both FE lagging frequencies deviate from the experimentally determined values. This discrepancy has to be further investigated, but it could have occurred as a consequence of the modelling approach, the test bench setup, the excitation direction or the age and unknown service history of the blade under test.

The natural frequencies determined from the FBG and DFOSS systems were compared against the uni-axial accelerometers. Only those modes that contain a flapping component could be compared, which highlights the need to use triaxial

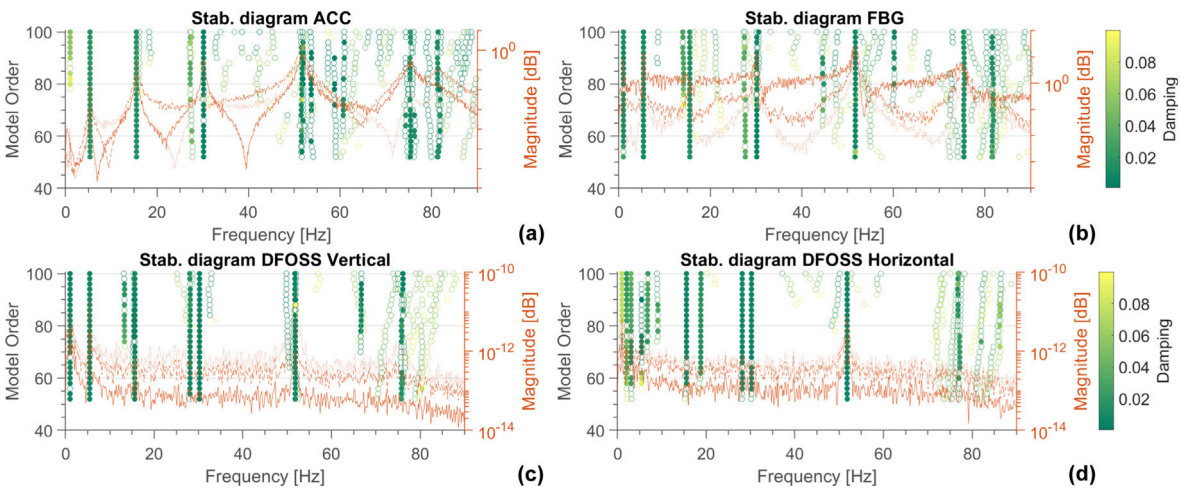

Fig. 13. Stabilisation diagrams computed with the following parameters: Δf = 0.5%, $\Delta\zeta$ = 5%, ΔMAC = 0.95 for one realisation of the: (a) ACC, (b) FBG, (c), and (d) DFOSS vertical and horizontal measurements.

Table 2
Natural frequency error of FBG and DFOSS instrumentation systems relative to the ACC measurements.

Mode number	Mode type	Error (%)	
		FBG vs ACC	DFOSS vs ACC
1	1st flapping	0.00	0.97
2	1st lagging	–	–
3	2nd flapping	0.19	1.47
4	3rd flapping	−0.52	0.83
5	2nd lagging	–	–
6	1st torsion	−0.92	−1.03
7	4th flapping	0.43	0.50
8	5th flapping	−0.25	−0.27
9	6th flapping	0.63	0.77
10	7th flapping	0.06	0.32

accelerometers for future testing. The relative errors, e, between the measured frequencies are listed in Table 2 and were calculated using Eq. (3):

$$e = \frac{f_X - f_R}{f_X} \tag{3}$$

where f_X and f_R are the experimentally determined frequencies and reference value, respectively. All the natural frequencies are in agreement with a percentage error of less than 1.50%. With the ACC data as the reference measurement, an average percentage error of the first eight natural frequencies of 0.38% for the FBG system, compared to that of 0.77% for the DFOSS system, suggests that the FBG system is able to characterise the natural frequencies more accurately.

3.4. Mode shape analysis

Both operational displacement and surface strain mode shapes were computed directly from the estimated state matrices determined using the output-only methodology described in the previous section. The FE displacement and strain mode shapes were used as a matter of comparison and analysis.

3.4.1. Displacement mode shapes

For the DFOSS mode shapes, an additional post-processing step is required, because the origin of the measurement at the first reflector R1 is located on the pitch control cuff, which can move relative to the blade mount. Unlike the FE model and the ACC measurements, which determine the shape of the blade relative to the fixed laboratory reference frame, the DFOSS reference frame, with its origin on the pitch control cuff itself, can be moving, which results in mode shapes that are apparently distorted. Therefore, the angle of the origin at R1 in the laboratory reference frame is unknown and has to be fitted as part of the correction procedure. In future implementations of this technique it would be advantageous to locate the origin reflector R1 of the DFOSS sensing cable directly on the blade mount to avoid this additional processing step.

The extracted DFOSS mode shapes are plotted in Fig. 14 as solid lines. Here, the unknown angle of the origin expresses itself though a distortion in the mode shapes that increases linearly with the blade radius. Through a visual fit with the FE model-generated mode shapes, shown in Fig. 15, the value of the slope angle of a straight line through the origin for each mode is found, which is subsequently subtracted from the measured mode shape to correct for the movement of the reference frame. The corrected mode shapes and the straight lines used for the correction are shown in Fig. 14. It should be noted that this post-processing step is a natural consequence of the movement of the reference frame and would not be necessary if R1 had been fixed. In future applications of the DFOSS method, the measurements will be referenced to a basis with a fixed angle, for example by mounting R1 on top of the rotor shaft, providing a stable origin.

Fig. 15 compares the displacement mode shapes predicted by the FE model with the corrected mode shapes obtained from the DFOSS system and the mode shapes determined from the ACC data. All mode shapes are normalised with respect to their maximum amplitude. Generally, good agreement between the model and the measurements can be observed. For the higher order modes, particularly for Mode 5F, the agreement seems to be reduced, with a phase shift of the mode shape visible at higher rotor radius values.

Closer investigation shows that this phase shift is a consequence of the spatial resolution of the DFOSS measurement and the error arising from the implemented spline interpolation in the DFOSS algorithm [47]. As previously mentioned, the output of the DFOSS system is the integration of interpolated slope angle curve, so the spatial resolution of the slope angle measurement needs to be sufficiently high to capture all relevant angular information. Fig. 16 compares the angle measurements and the interpolated slope angle curve with the first derivative of the FE mode shape. The plot shows that the actual angle measurements at locations R2 to R7 agree well with the calculated local FE slope values, however, the interpolated slope angle curve deviates from the FE model between measurement points. It can therefore be concluded from Fig. 16 that, in

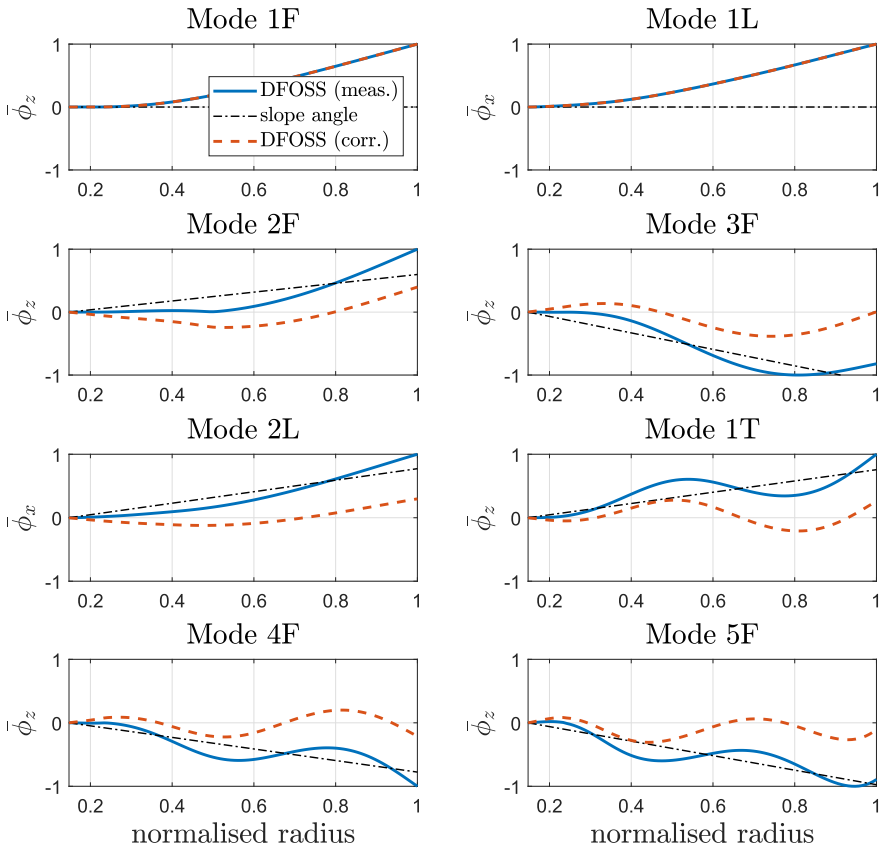

Fig. 14. Measured DFOSS mode shapes versus corrected DFOSS mode shape. The DFOSS horizontal component is used for the lagging modes, otherwise the vertical component is used.

the case of Mode 5F, the observed phase shift in Fig. 15 is a result of an interpolation error due to the limited number of measurement points. The spatial resolution of the DFOSS measurement is therefore insufficient and the density of reflectors would need to be increased to confidently reproduce this mode shape.

3.4.2. Strain mode shapes

The FBG array mounted on the lower surface on the mid-chord line (Array E in Fig. 7(d)) was used to obtain the flapping and torsional strain mode shapes, while the array on the lower surface trailing edge (Array F in Fig. 7(d)) was used to obtain the lagging strain mode shapes, as these provided the highest signal-to-noise ratios. Fig. 17 presents the comparison of the FBG-derived strain mode shapes with the strain mode shapes, $\bar{\psi}$, determined from the FE model, where both strain mode shapes were normalised to their maximum amplitude. In general there is good agreement, despite some discontinuities that could be due to numerical errors generated from the second spatial differentiation of the calculated mode shapes. Furthermore, a sudden change in strain mode shape is evident, in particular for Mode 3F at 24% rotor radius, approximately the location where the pitch control cuff merges with the main structure of the blade. This behaviour is well captured by both the analytical and experimental mode shapes, and demonstrates the sensitivity of strain measurements to the exact sensor location. This highlights the need to exercise caution when selecting the locations for the FBG sensors and the need to verify the correct placement of the sensors on the blade.

3.4.3. Modal Assurance Criterion Analysis

The analytically and experimentally determined mode shapes were assessed using the Modal Assurance Criterion (MAC) [1], where a MAC value between 0.9–1 is obtained for well-correlated modes, while a low MAC value is an indication of uncorrelated modes. Table 3 compares the MAC computed using FE and the experimentally determined mode shapes from ACC, FBG and, DFOSS systems.

A match between ACC determined mode shapes and the FE model is obtained, with MAC values greater than 0.8. From the FBG measurements, an overall agreement is attained with a pairing of MAC $>$ 0.77, except for Mode 1T where MAC = 0.58. Reasons for this discrepancy, in particular for the first strain measurement at approximately 10% rotor radius, could be due to the assumptions made in the mathematical formulation as explained in Section 2. The mode shape pairing achieved with the

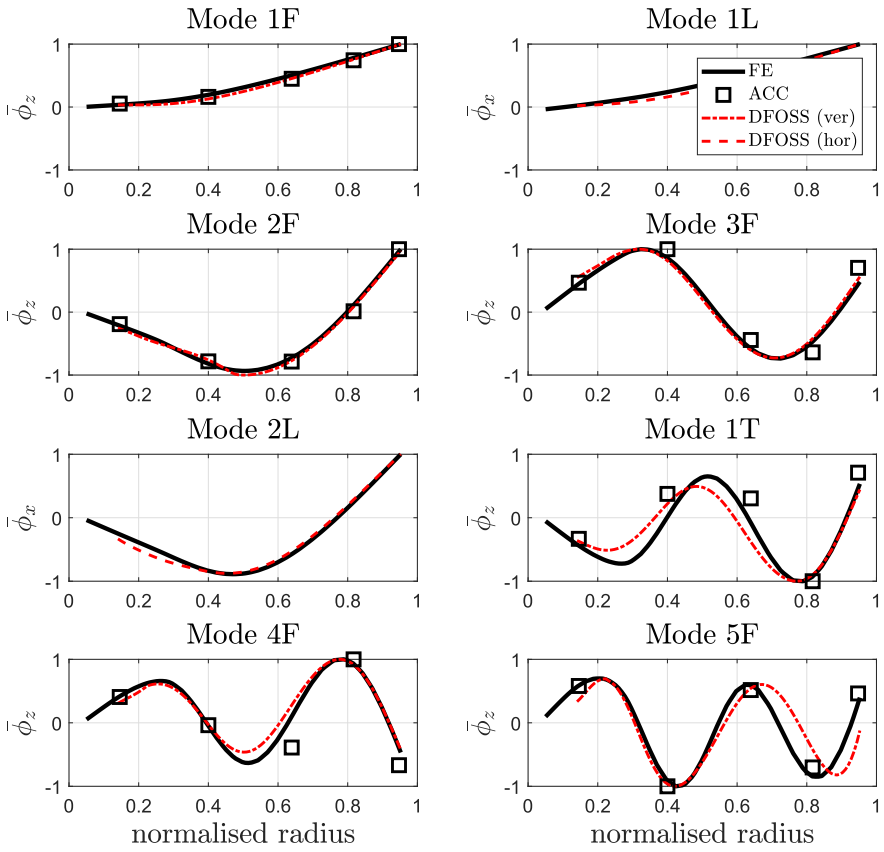

Fig. 15. Comparison of normalised displacement mode shapes $\bar{\phi}$.

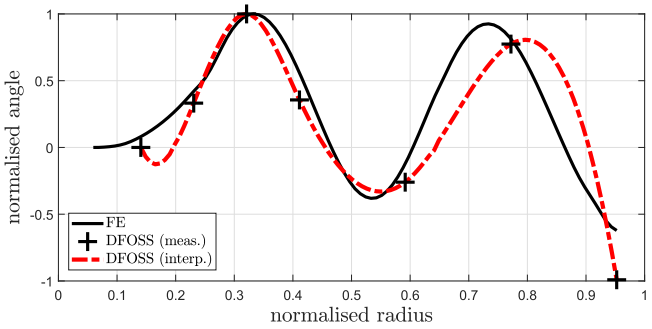

Fig. 16. Comparison of normalised angle measurements, the chosen slope angle interpolation and the slope angle curve calculated from the FE model for Mode 5F.

DFOSS system resulted in a MAC $\geqslant$ 0.89, discounting the lower MAC value of MAC = 0.78 for Mode 5F due to the insufficient spatial resolution as explained previously.

4. Conclusions & further work

This paper compared the performances of two state-of-the-art optical fibre based techniques for characterising the structural dynamics of a helicopter blade, one based on the measurement of strain and the other on the direct measurement of slope angle, from which the shape could be determined. This was achieved through a series of GVT, using accelerometers and an baseline FE model as references. It was found that for FBG-based strain measurements the sensitivities to the modes were dependent upon the location of the sensor element relative to the neutral axes of the structure, suggesting that full modal

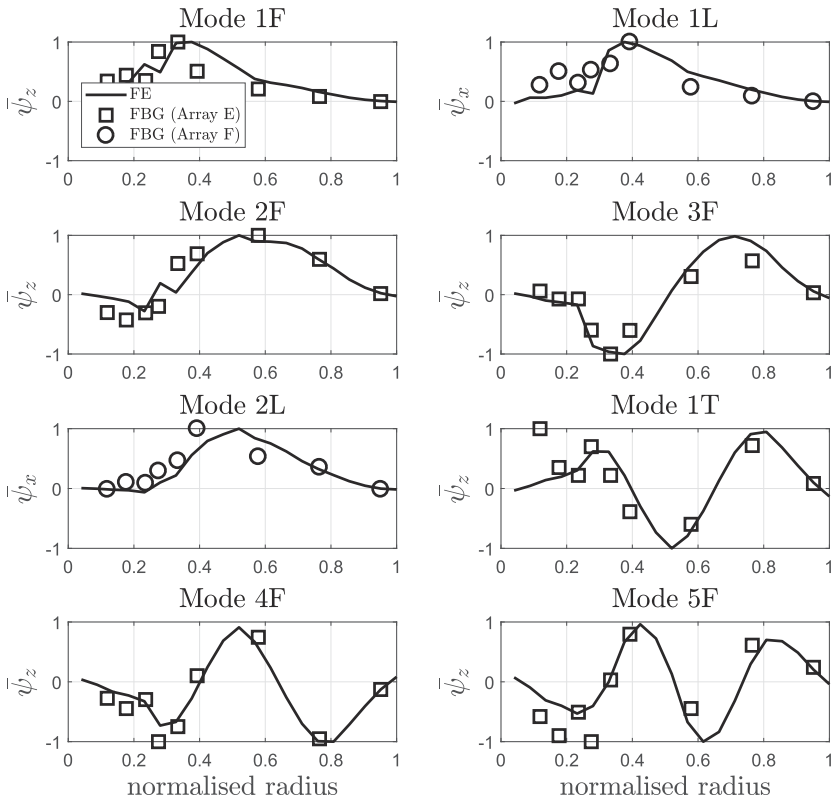

Fig. 17. Comparison of normalised strain mode shapes $\bar{\psi}$ determined by the FBG strain measurements and the output from the FE model.

Table 3
Comparison of mode shape pairing with FE model.

Mode	Mode	MAC		
number	type	ACC	FBG	DFOSS
1	1st flapping	1.00	0.83	0.99
2	1st lagging	–	0.77	0.99
3	2nd flapping	1.00	0.80	1.00
4	3rd flapping	0.96	0.94	0.99
5	2nd lagging	–	0.81	0.99
6	1st torsion	0.81	0.58	0.89
7	4th flapping	0.83	0.94	0.97
8	5th flapping	0.98	0.78	0.78

identification would require careful optimisation of the distribution of the sensors, with knowledge of the underlying structure. DFOSS, on the other hand, by virtue of its high sensitivity and the two-dimensional measurement capability, allowed the resonance frequencies of the flapping, lagging and torsional modes to be measured using a single sensing cable. Furthermore, the results showed that the signal-to-noise ratio of the FBG measurement is considerably lower than those of the DFOSS and ACC measurements. The high repeatability of the experimentally determined natural frequencies contributes to the confidence in both FBG and DFOSS systems for characterising structural dynamics. While the natural frequencies obtained from FBG and DFOSS are in good agreement, with a percentage error of less than 1.50%, the FBG measurements provided the more accurate results when benchmarked against the natural frequencies obtained from ACC data. On the other hand, a closer match between FE-calculated mode shapes and the DFOSS system of MAC $\geqslant$ 0.89 (for the first seven modes) was achieved, compared to results obtained from the FBG sensors. Although the FBG strain mode shapes in the flapping and lagging direction are in agreement of MAC $>$ 0.77, a lower value of MAC = 0.58 for Mode 1T resulted from the FE model limitation that neglected shear strain.

Both instrumentation systems show the potential for characterising structural blade dynamics in a controlled laboratory environment. The final step of the BladeSense project [51] is to demonstrate the capability of the developed technologies in a

rotating environment on a working helicopter. The long term aim is to adopt such fibre optic instrumentation systems for operational flight with the purpose of reducing maintenance costs and providing much needed operational data on helicopter blade dynamics to validate methods and improve designs.

CRediT authorship contribution statement

Simone Weber: Conceptualization, Methodology, Software, Validation, Formal analysis, Investigation, Data curation, Writing - original draft, Visualization. **Thomas Kissinger:** Conceptualization, Methodology, Software, Validation, Investigation, Data curation, Writing - review & editing, Visualization. **Edmond Chehura:** Methodology, Investigation. **Stephen Staines:** Methodology, Investigation. **James Barrington:** Methodology, Investigation. **Kevin Mullaney:** Methodology, Investigation. **Luca Zanotti Fragonara:** Software, Validation, Formal analysis, Data curation, Writing - review & editing, Visualization. **Ivan Petrunin:** Software, Formal analysis. **Stephen James:** Conceptualization, Methodology, Investigation, Data curation, Writing - review & editing, Supervision. **Mudassir Lone:** Conceptualization, Methodology, Software, Writing - review & editing, Supervision, Project administration, Funding acquisition. **Ralph Tatam:** Conceptualization, Methodology, Writing - review & editing, Supervision, Project administration, Funding acquisition.

Declaration of Competing Interest

The authors declare that they have no known competing financial interests or personal relationships that could have appeared to influence the work reported in this paper.

Acknowledgements

The authors would like to acknowledge funding from Innovate UK via the Aerospace Technology Institute (ATI) as part of the BladeSense project (ATI 102381). We also acknowledge funding from the Engineering and Physical Sciences Research Council (EPSRC) UK via grant EP/N002520/1. The underlying data can be accessed from the Cranfield Online Research Data Repository at https://doi.org/ 10.17862/cranfield.rd.13806794.

References

[1] D. Ewins, Modal Testing – Theory, Practice and Application, second ed., Research Studies Press Ltd., Exeter, Great Britian, 2000.
[2] P. Avitabile, Modal Testing. A Practitioner's Guide, John Wiley & Sons Ltd, USA, 2018.
[3] M. Martinez, M. Yanishevsky, B. Rocha, R.M. Groves, N. Bellinger, Maintenance and Monitoring of Composite Helicopter Structures and Materials, Elsevier Ltd., 2015.
[4] P.M. Pawar, R. Ganguli, Helicopter rotor health monitoring – a review, Proceedings of the Institution of Mechanical Engineers, Part G: Journal of Aerospace Engineering 221 (5) (2007) 631–647.
[5] V. Giurgiutiu, Structural health monitoring (SHM) of aerospace composites, Polymer Composites in the Aerospace Industry (2014) 449–507.
[6] D. Lombardo, Helicopter structures – a review of loads, fatigue, design techniques and usage monitoring, Tech. Rep. ARL-TR-15, Defence Science and Technology Organisation, Melbourne, Australia, Department of Defence, 1993..
[7] A.I. Abrego, L.E. Olson, E.A. Romander, D.A. Barrows, A.W. Burner, Blade displacement measurement technique applied to a full-scale rotor test, in: 68th American Helicopter Society International Annual Forum, 1–3 May, Texas, USA 4, 2012, pp. 2771–2794.
[8] D.C. Kammer, M.L. Tinker, Optimal placement of triaxial accelerometers for modal vibration tests, Mechanical Systems and Signal Processing 18 (1) (2004) 29–41.
[9] F.L.M. dos Santos, B. Peeters, H. van der Auweraer, L.C.S. Góes, W. Desmet, Vibration-based damage detection for a composite helicopter main rotor blade, Case Studies in Mechanical Systems and Signal Processing 3 (2016) 22–27.
[10] S. Stupar, A. Simonović, M. Jovanović, Measurement and analysis of vibrations on the helicopter structure in order to detect defects of operating elements, Scientific Technical Review 62 (1) (2012) 58–63.
[11] R. Golub, W. McLachlan, In-flight measurement of rotor blade airloads, bending moments, and motions, together with rotor shaft loads and fuselage vibration, on a tandem rotor helicopter. Volume I. Instrumentation and in-flight recording system, Tech. Rep. 67-9A, U.S. Army Aviation Materiel Laboratories, Virginia, USA, 1967..
[12] W.J. Grant, R.R. Pruyn, In-flight measurement of rotor blade airloads, bending moments, and motions, together with rotor shaft loads and fuselage vibration, on a tandem rotor helicopter. Volume II. Calibrations and instrumented component testing., Tech. Rep. 67-9B, U.S. Army Aviation Materiel Laboratories, Virginia, USA, 1967..
[13] J. Riley, G.D. Padfield, J. Smith, Estimation of rotor blade incidence and blade deformation from the measurement of pressures and strains in flight, in: 14th European Rotorcraft Forum, Milano, Italy, 1988, pp. 1–20.
[14] A. Datta, I. Chopra, Validation of structural and aerodynamic modeling using UH-60A airloads program data, Journal of the American Helicopter Society 51 (1) (2006) 43–58.
[15] R. Steijl, G.N. Barakos, K.J. Badcock, Computational study of the advancing-side lift-phase problem, Journal of Aircraft 45 (1) (2008) 246–257.
[16] G.C. Foss, E.D. Haugse, Using modal test results to develop strain to displacement transformations, in: Proc. SPIE Vol. 2460, Proceedings of the 13th International Modal Analysis Conference, 1995, pp. 112–118..
[17] C.J. Li, A.G. Ulsoy, High-precision measurement of tool-tip displacement using strain gauges in precision flexible line boring, Mechanical Systems and Signal Processing 13 (1999) 531–546.
[18] W.L. Ko, W.L. Richards, U.S. Patent application for "Method for real-time structure shape-sensing", 2009..
[19] M.J. Nicolas, R.W. Sullivan, W.L. Richards, Large scale applications using FBG sensors: determination of in-flight loads and shape of a composite aircraft wing, Aerospace 3 (3) (2016) 1–15.
[20] G. Sun, Y. Wu, H. Li, L. Zhu, 3D shape sensing of flexible morphing wing using fiber Bragg grating sensing method, Optik 156 (2018) 83–92.
[21] G. Bernardini, R. Porcelli, J. Serafini, P. Masarati, Rotor blade shape reconstruction from strain measurements, Aerospace Science and Technology 79 (2018) 580–587.
[22] J. Sirohi, M.S. Lawson, Measurement of helicopter rotor blade deformation using digital image correlation, Optical Engineering 51 (4) (2012) 1–8.
[23] K. von Gersdorff, K. Knobling, Die deutsche Luftfahrt. Hubschrauber und Tragschrauber, third edition., Bernard & Graefe Verlag, 1999..

[24] G.A. Fleming, S.A. Gorton, Measurement of rotorcraft blade deformation using Projection Moiré interferometry, Shock and Vibration 7 (3) (2000) 149–165.
[25] O. Schneider, B.G. van der Wall, K. Pengel, HART II blade motion measured by Stereo Pattern Recognition (SPR), in: American Helicopter Society 59th Annual Forum, 6-8 May, Arizona, USA, 2003, pp. 1–14.
[26] D.H. Kim, S.H. Kim, J.W. Park, J.H. Han, Blade deformation measurement of a model-scale rotor system using a SPR system with IR cameras, in: 39th European Rotorcraft, 3–6 September, Moscow, Russia, 2013, pp. 458–466.
[27] S. Rizo-Patron, J. Sirohi, Operational modal analysis of a rotating cantilever beam using high-speed digital image correlation, in: 57th AIAA/ASCE/AHS/ASC Structures, Structural Dynamics, and Material Conference, 4–8 January, California, USA, 2016, pp. 1–19.
[28] B. Stasicki, F. Boden, Application of high-speed videography for in-flight deformation measurements of aircraft propellers, in: 28th International Congress on High-Speed Imaging and Photonics, 9–14 November, Canberra, Australia 7126, 2008, pp. 1–12.
[29] R. Boden, A. Torres, C. Maucher, Advanced optical rotor blade deformation measurements on a flying helicopter, in: 35th European Rotorcraft Forum, 22-25 September, Hamburg, Germany 1, 2009, pp. 218–227.
[30] C. Maucher, F. Boden, Blade deformation measurements with IPCT on an EC 135 helicopter rotor, Advanced in-flight Measurement Techniques (2013) 196–212.
[31] F. Boden, B. Stasicki, Non-intrusive in-flight propeller blade deformation measurements by means of a rotating camera, in: 34th European Telemetry and Test Conference, 2014, pp. 58–63.
[32] F. Boden, B. Stasicki, K. Ludwikowski, Optical rotor-blade deformation measurements using a rotating camera, in: 38th European Test and Telemetry Conference, 26–28 June, Nuremberg, Germany, 2018, pp. 147–154.
[33] R. Di Sante, Fibre optic sensors for structural health monitoring of aircraft composite structures: recent advances and applications, Sensors 15 (8) (2015) 18666–18713.
[34] G. Dell'Anno, I. Partridge, D. Cartié, A. Hamlyn, E. Chehura, S.W. James, R.P. Tatam, Automated manufacture of 3D reinforced aerospace composite structures, International Journal of Structural Integrity 3 (1) (2012) 22–40.
[35] E. Chehura, R. Jarzebinska, E.F.R. Da Costa, A.A. Skordos, S.W. James, I.K. Partridge, R.P. Tatam, Multiplexed fibre optic sensors for monitoring resin infusion, flow, and cure in composite material processing, Proceedings of SPIE – The International Society for Optical Engineering 8693 (March) (2013) 86930F.
[36] L.M. Bottasso, G. Sala, P., Bettini, P. Tagliabue, F., Corbani, E. Platini, A. Guerra, A. Anelli, A rugged fiber optics monitoring system for helicopter rotor blades, in: 44th European Rotorcraft Forum, 18–21 September, Delft, The Netherlands, 2018, pp. 1–16..
[37] N.J. Lawson, R. Correia, S.W. James, M. Partridge, S.E. Staines, J.E. Gautrey, K.P. Garry, J.C. Holt, R.P. Tatam, Development and application of optical fibre strain and pressure sensors for in-flight measurements, Measurement Science and Technology 27 (10) (2016) 1–17.
[38] S.J. Buggy, S.W. James, S.E. Staines, R. Carroll, P.V. Kitson, D. Farrington, L. Drewett, J. Jaiswal, R.P. Tatam, Railway track component condition monitoring using optical fibre Bragg grating sensors, Measurement Science and Technology 27 (5) (2016) 1–15.
[39] R.M. Groves, E. Chehura, W. Li, S.E. Staines, S.W. James, R.P. Tatam, Surface strain measurement: a comparison of speckle shearing interferometry and optical fibre Bragg gratings with resistance foil strain gauges, Measurement Science and Technology 18 (5) (2007) 1175–1184.
[40] A. Cusano, A. Cutolo, J. Albert, Fiber Bragg grating sensors: recent advancements, industrial applications and market exploitation, Bentham Science Publishers, Oxford, 2018.
[41] C.V. Jutte, W.L. Ko, C.A. Stephens, J.A. Bakalyar, W.L. Richards, A.R. Parker, Deformed shape calculation of a full-scale wing using fiber optic strain data from a ground loads test, Tech. Rep. NASA/TP-2011-215975, NASA Dryden Flight Research Centre, California, USA, 2011..
[42] S.B. Kim, D. Geiger, P.O. Bowles, C.G. Matalanis, B.E. Wake, Tip displacement estimation using fiber optic sensors for X2 technology™ rotor blades, in: AHS International 72nd Annual Forum, 16-19 May, West Palm Beach, Florida, USA 3, 2016, pp. 1914–1923.
[43] M. Hajek, S. Manner, S. Süße, Blade root integrated optical fiber Bragg grating sensors – a highly redundant data source for future HUMS, in: AHS International 71st Annual Forum, 5-7 May, Virginia Beach, Virginia, USA 3, 2015, pp. 1598–1605.
[44] J. Serafini, G. Bernardini, I. Mattioni, V. Vezzari, C. Ficuciello, Non-invasive dynamic measurement of helicopter blades, Journal of Physics: Conference Series 882 (2017) 1–12.
[45] P.M. Blanchard, J.G. Burnett, G.R.G. Erry, A.H. Geenaway, P. Harrison, B. Mangan, J.C. Knight, P.St.J. Russel, M.J. Gander, R. McBridge, J.D.C. Jones, Two-dimensional bend sensing with a single, multi-core optical fibre, Smart Materials and Structures 2 (9) (2000) 132–140..
[46] T. Loutas, A. Bourikas, Strain sensors optimal placement for vibration-based structural health monitoring. The effect of damage on the initially optimal configuration, Journal of Sound and Vibration 410 (1) (2017) 217–230.
[47] T. Kissinger, E. Chehura, S.E. Staines, S.W. James, R.P. Tatam, Dynamic fiber-optic shape sensing using fiber segment interferometry, Journal of Lightwave Technology 36 (4) (2018) 917–925.
[48] F. Jülich, L. Aulbach, A. Wilfert, P. Kratzer, R. Kuttler, J. Roths, Gauge factors of fibre Bragg grating strain sensors in different types of optical fibres, Measurement Science and Technology 24 (9)..
[49] R.G. Duncan, M.E. Froggatt, S.T. Kreger, R.J. Seeley, D.K. Gifford, A.K. Sang, M.S. Wolfe, High-accuracy fiber-optic shape sensing, in: K.J. Peters (Ed.), Sensor Systems and Networks: Phenomena, Technology, and Applications for NDE and Health Monitoring 2007, vol. 6530, International Society for Optics and Photonics, SPIE, 2007, pp. 487–497.
[50] A. Zafeiropoulou, A. Masoudi, A. Zdagkas, L. Cooper, G. Brambilla, Curvature sensing with a d-shaped multicore fibre and brillouin optical time-domain reflectometry, Optics Express 28 (2) (2020) 1291–1299.
[51] S. Weber, D. Southgate, K. Mullaney, S.W. James, R.Rutherford, A. Sharma, M.M. Lone, T. Kissinger, E. Chehura, S. Staines, H. Pekmezci, L. Zanotti Fragonara, I. Petrunin, D. Williams, I. Moulitsas, A. Cooke, N. Lawson, W. Rosales, R.P. Tatam, P. Morrish, M. Fairhurst, R. Atack, G. Bailey, S. Morley, BLADESENSE – A novel approach for measuring dynamic helicopter rotor blade deformation, in: 44th European Rotorcraft Forum, 18-21 September, Delft, The Netherlands, 2018, pp. 1–7..
[52] H. Bansemir, R. Müller, The EC135 – Applied Advanced Technology, in: 53rd Annual Forum Proceedings - AHS International, 29 April - 1 May, Virginia, USA 2, 1997, pp. 846–861.
[53] H. Bansemir, S. Emmerling, Fatigue substantiation and damage tolerance evaluation of fiber composite helicopter components, in: RTO AVT Specialists' Meeting on "Application of Damage Tolerance Principles for Improved Airworthiness of Rotorcraft", 21–22 April 1999, Corfu, Greece, 1999, pp. 1–11..
[54] K. Kampa, B. Enenkl, G. Polz, G. Roth, Aeromechanic aspects in the design of the EC135, Journal of the American Helicopter Society 44 (2) (1997) 83–93.
[55] MSC Nastran. Finite Element Analysis (FEA) solver, http://www.dte.co.uk/msc-nastran/, accessed on 24 July 2019..
[56] R. Bielawa, Rotary Wing Structural Dynamics and Aeroelasticity, second ed., American Institute of Aeronautics and Astronautics Inc., USA, 2006.
[57] T. Kissinger, R. Correia, T.O.H. Charrett, S.W. James, R.P. Tatam, Fibre segment interferometry for dynamic strain measurements, Journal of Lightwave Technology 34 (19) (2016) 4620–4626.
[58] T. Kissinger, T.O.H. Charrett, R.P. Tatam, Range-resolved interferometric signal processing using sinusoidal optical frequency modulation, Optics Express 23 (7) (2015) 9415–9431.
[59] Y. Rao, In-fibre Bragg grating sensors, Measurement Science and Technology 8 (4) (1997) 355–375.
[60] P. Welch, The use of fast transform for the estimation of power spectra: a method based on time averaging over short, modified periodograms, IEEE Transactions on Audio and Electroacoustics 15 (2) (1967) 70–73.
[61] P. Van Overschee, B. De Moor, Subspace Identification for Linear Systems: Theory and Implementation – Applications, Kluwer Academic Press, Dordrecht, 1996.
[62] E. Neu, F. Janser, A.A. Khatibi, A.C. Orifici, Fully automated operational modal analysis using multi-stage clustering, Mechanical Systems and Signal Processing 84 (2017) 308–323.

2021-03-09

Application of fibre optic sensing systems to measure rotor blade structural dynamics

Weber, Simone

Elsevier

Weber S, Kissinger T, Chehura E, et al., (2021) Application of fibre optic sensing systems to measure rotor blade structural dynamics. Mechanical Systems and Signal Processing, Volume 158, September 2021, Article number 107758

https://doi.org/10.1016/j.ymssp.2021.107758